Geostationary observations of atmospheric ammonia over East Asia:

spatio-temporal variations revealed by three years of FY-4B/GIIRS

measurements

- Mengya Sheng¹, Runyi Zhou¹, Jiancong Hua¹, Shan Han¹, Shangyi Liu¹, Lin Zhang², Wei Wang³, Ruijun
- Dang⁴, Hansen Cao⁵, Zichong Chen⁶, Yixuan Gu⁷, Mingxu Liu⁸, Lu Lee⁹, Chengli Qi⁹, Feng Lu⁹, 5
- Changpei Han¹⁰, Mark W. Shephard¹¹, Nadir Guendouz¹², Camille Viatte¹², Lieven Clarisse¹³, Martin Van Damme^{13,14}, Cathy Clerbaux^{12,13}, Zhao-Cheng Zeng^{1,*}
- 7
- 8 ¹ School of Earth and Space Sciences, Peking University, Beijing 100871, China
- 9 ² Laboratory for Climate and Ocean-Atmosphere Studies, Department of Atmospheric and Oceanic Sciences, School of Physics,
- 10 Peking University, Beijing 100871, China
- 11 ³ Key Laboratory of Environmental Optics and Technology, Anhui Institute of Optics and Fine Mechanics, Chinese Academy 12 of Sciences, Hefei 230031, China
- 13 ⁴ School of Engineering and Applied Sciences, Harvard University, Cambridge, MA 02138, USA
- 14 ⁵ School of Environmental Science and Engineering, Southern University of Science and Technology, Shenzhen, Guangdong 15 518055, China
- 16 ⁶ Hong Kong University of Science and Technology, Guangzhou 511400, China
- 17 ⁷ Jiangsu Key Laboratory of Atmospheric Environment Monitoring and Pollution Control, Collaborative Innovation Center of
- 18 Atmospheric Environment and Equipment Technology, Joint International Research Laboratory of Climate and Environment
- 19 Change, School of Environmental Science and Engineering, Nanjing University of Information Science and Technology,
- 20 Nanjing 210044, China
- 21 ⁸ College of Environmental Sciences and Engineering, Peking University, Beijing 100871, China
- 22 ⁹ Key Laboratory of Radiometric Calibration and Validation for Environmental Satellites, National Satellite Meteorological $\overline{23}$ Center, China Meteorological Administration, Beijing 100081, China
- 24 ¹⁰Key Laboratory of Infrared Science and Technology, Shanghai Institute of Technical Physics, Chinese Academy of Sciences, 25 Shanghai 200083, China
- 26 ¹¹ Environment and Climate Change Canada, Toronto, Ontario M3H 5T4, Canada
- 27 ¹² LATMOS/IPSL, Sorbonne Université, UVSQ, CNRS, Paris 75252, France
- 28 ¹³ Spectroscopy, Quantum Chemistry and Atmospheric Remote Sensing (SQUARES), Brussels Laboratory of the Universe
- 29 (BLU-ULB), Université libre de Bruxelles (ULB), Brussels 1050, Belgium
- 30 ¹⁴ Royal Belgian Institute for Space Aeronomy, Brussels 1180, Belgium 31

32 Text S1 Calculation of the modelled NH₃ columns by applying satellite AVKs to GEOS-CF NH₃

33 profiles

In this study, GEOS-CF model data were used as a consistent and comparable reference to account for the vertical sensitivity of the satellite retrievals. The satellite retrievals operate on different vertical layers (GIIRS: ~12 layers; IASI: ~14 layers; CrIS: ~14 layers). The GEOS-CF NH₃ profiles collocated with the satellite observations were interpolated onto the instrument-specific retrieval layers. The GEOS-CF NH₃ profiles were initially interpolated onto each instrument's retrieval grid. Subsequently, the profiles were converted to total columns by using the satellite averaging kernels (AVKs) and a priori profiles according to the following equation:

$$\widehat{M}_{AK,sat} = \sum_{z} A_z^{sat} (M_z^{model} - B_z) + B$$

where M_z^{model} represents GEOS-CF NH₃ profiles that have been interpolated onto the satellite-retrieved layer (z), A_z^{sat} is the satellite AVSs, B_z is the a priori profile used in the retrieval algorithm, and B corresponds to the total column associated with B_z . The resulting modelled NH₃ columns $\widehat{M}_{AK,sat}$ are hereafter referred to as GEOS-CF_{AK, GIIRS}, GEOS-CF_{AK, GIIRS}, and GEOS-CF_{AK, GIIRS} for GIIRS, IASI, and CrIS, respectively. As shown in Fig. S1, the a priori profile used in the IASI retrievals follows the method described in Clarisse et al., (2023), which provides only the vertical profile shape. In the calculation for IASI, B_z is assumed to be zero.

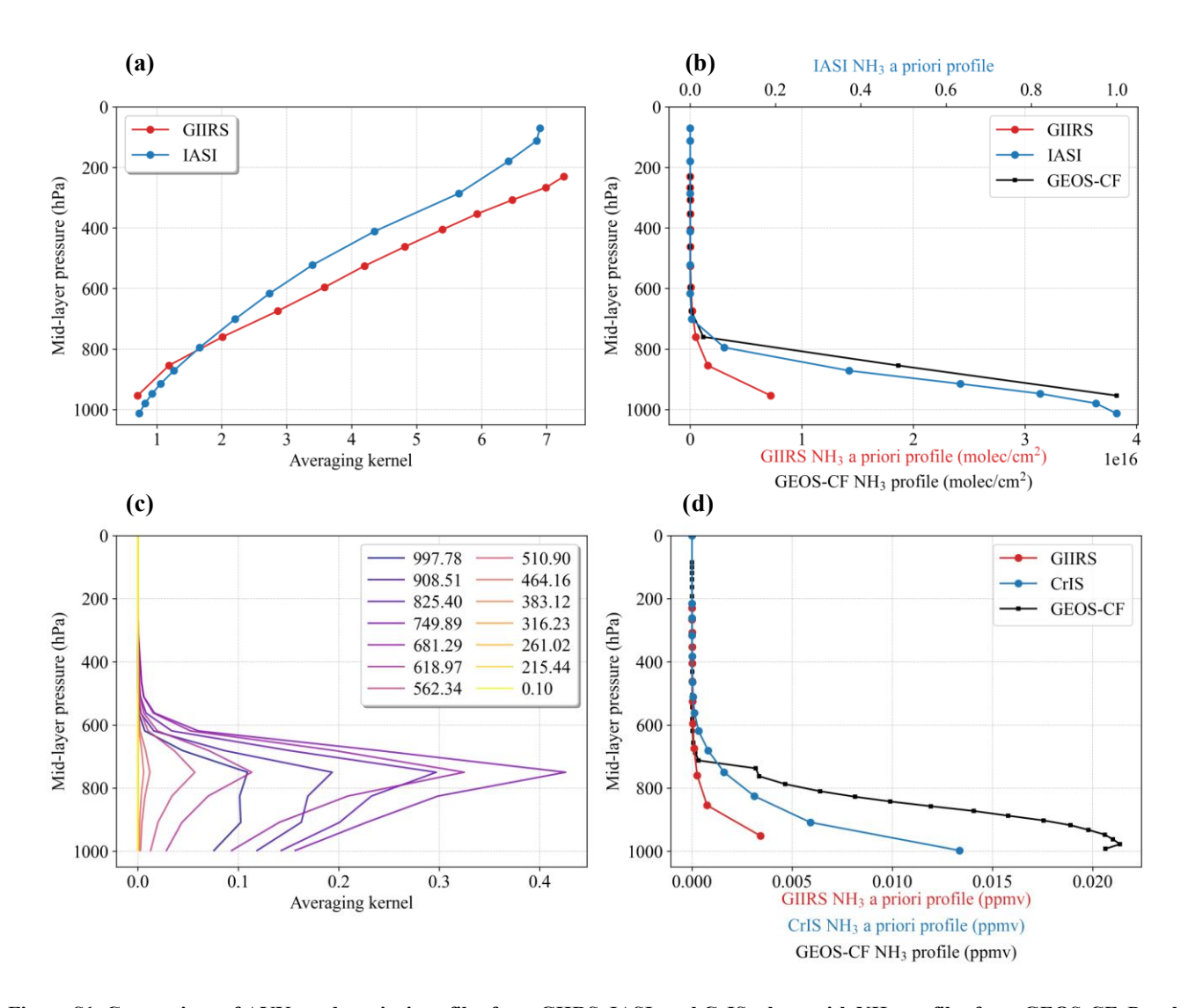


Figure S1. Comparison of AVKs and a priori profiles from GIRS, IASI, and CrIS, along with NH₃ profiles from GEOS-CF. Panels (a) and (b), and (c) and (d) show two example retrievals over the A1 area in the North China Plain on 9 June 2024 and 14 June 2024, respectively. (a) is satellite's AVKs from GIRS and IASI. (b) is the a priori profile from GIRS and IASI, and GEOS-CF NH₃ profile that have been interpolated onto GIRS' retrieved layers. (c) is the a priori profile from CrIS at the corresponding rows of AVKs. (d) is similar to (a) but for GIRS, CrIS, and GEOS-CF without interpolating. For GIRS, retrievals are performed below 200 hPa, and a single a priori profile is applied to all observations, in which the lowest layer is adjusted by interpolating to the surface pressure obtained from ERA5.

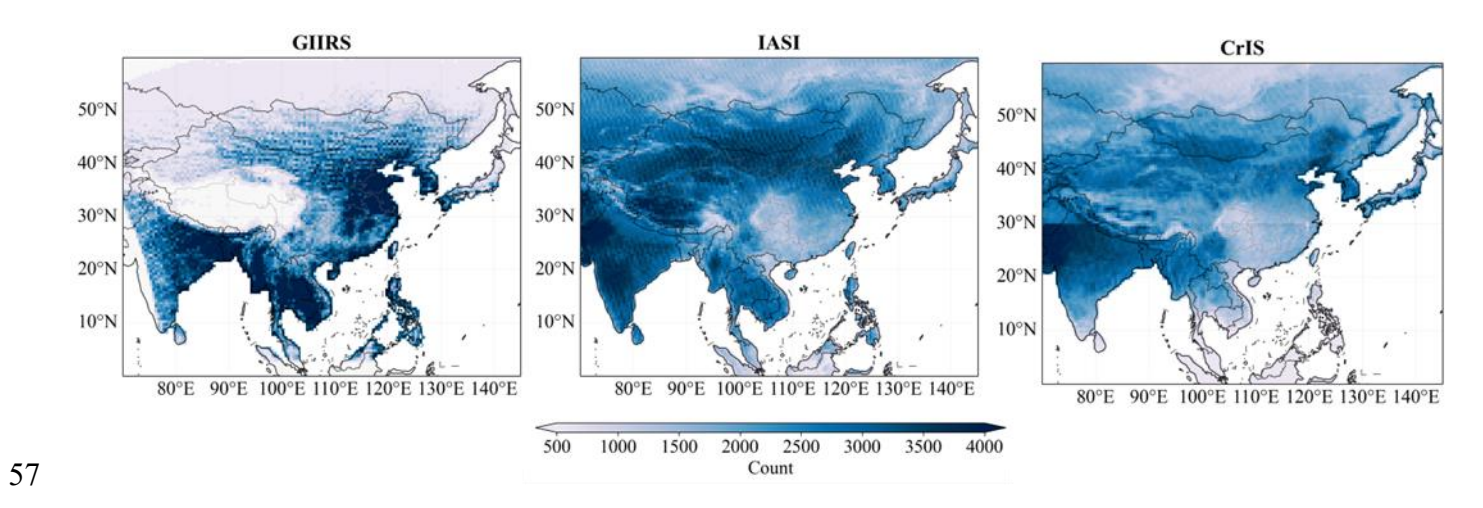


Figure S2. The valid data points of satellite NH₃ retrievals from July 2022 to June 2025 for GIIRS and IASI, and from July 2022 to April 2025 for CrIS at a spatial scale of 0.5°×0.5° grid.

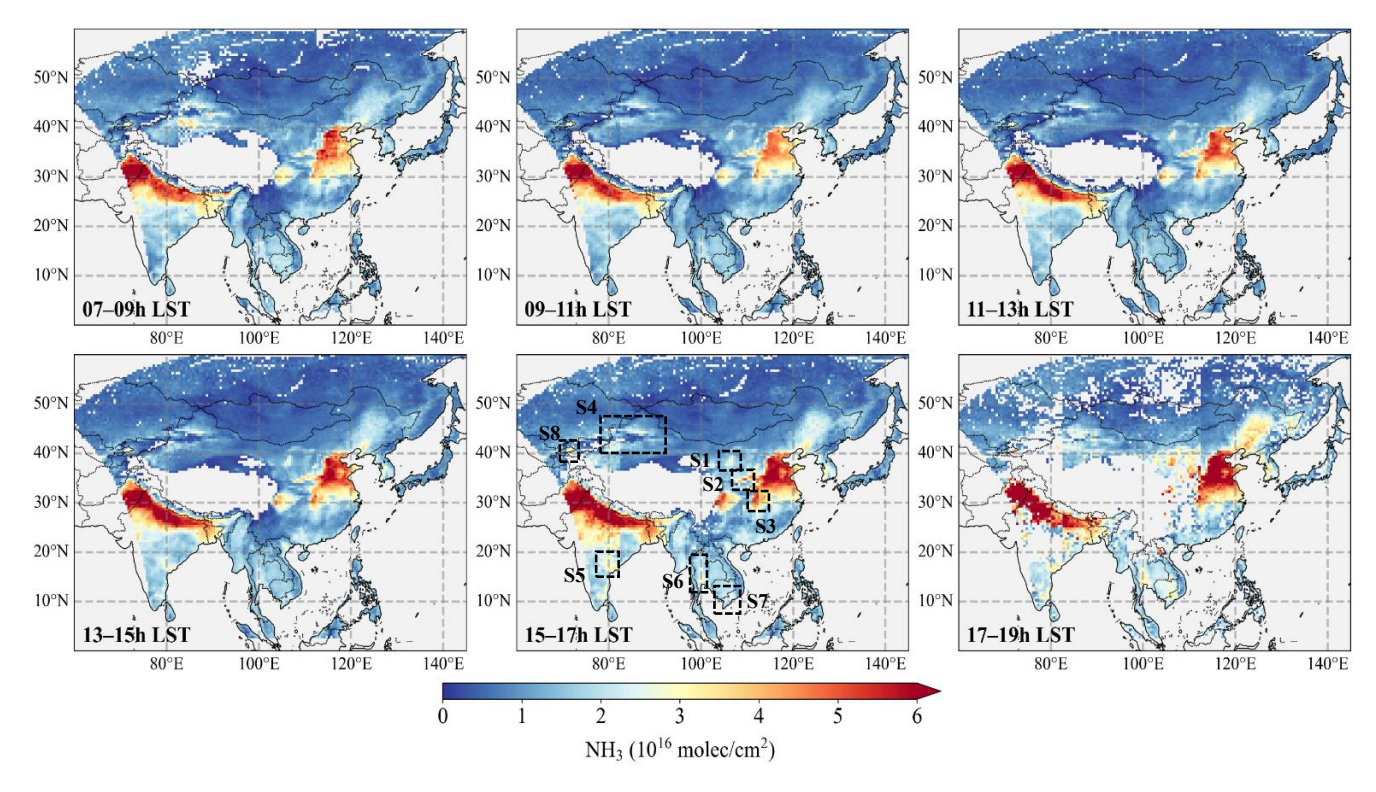


Figure S3. Three-year mean NH₃ columns retrieved from FY-4B/GIIRS observations between July 2022 and June 2025. The maps are displayed on a $0.5^{\circ} \times 0.5^{\circ}$ grid at two-hour intervals, starting at local solar times of 07:00, 09:00, 11:00, 13:00, 15:00, and 17:00. Grid cells with less than 10 data points were excluded. The dashed boxes denote regions exhibiting localized enhancements of NH₃ columns: the Ningxia Irrigation Plain (S1), the Wei River Plain (S2), the Jianghan Plain (S3), and oasis agriculture in the arid regions of Xinjiang (S4), the central Deccan Plateau in India (S5), the Mekong Delta in Vietnam (S6), the Chao Phraya River Plain in Thailand (S7), and the Fergana Valley in Uzbekistan (S8).

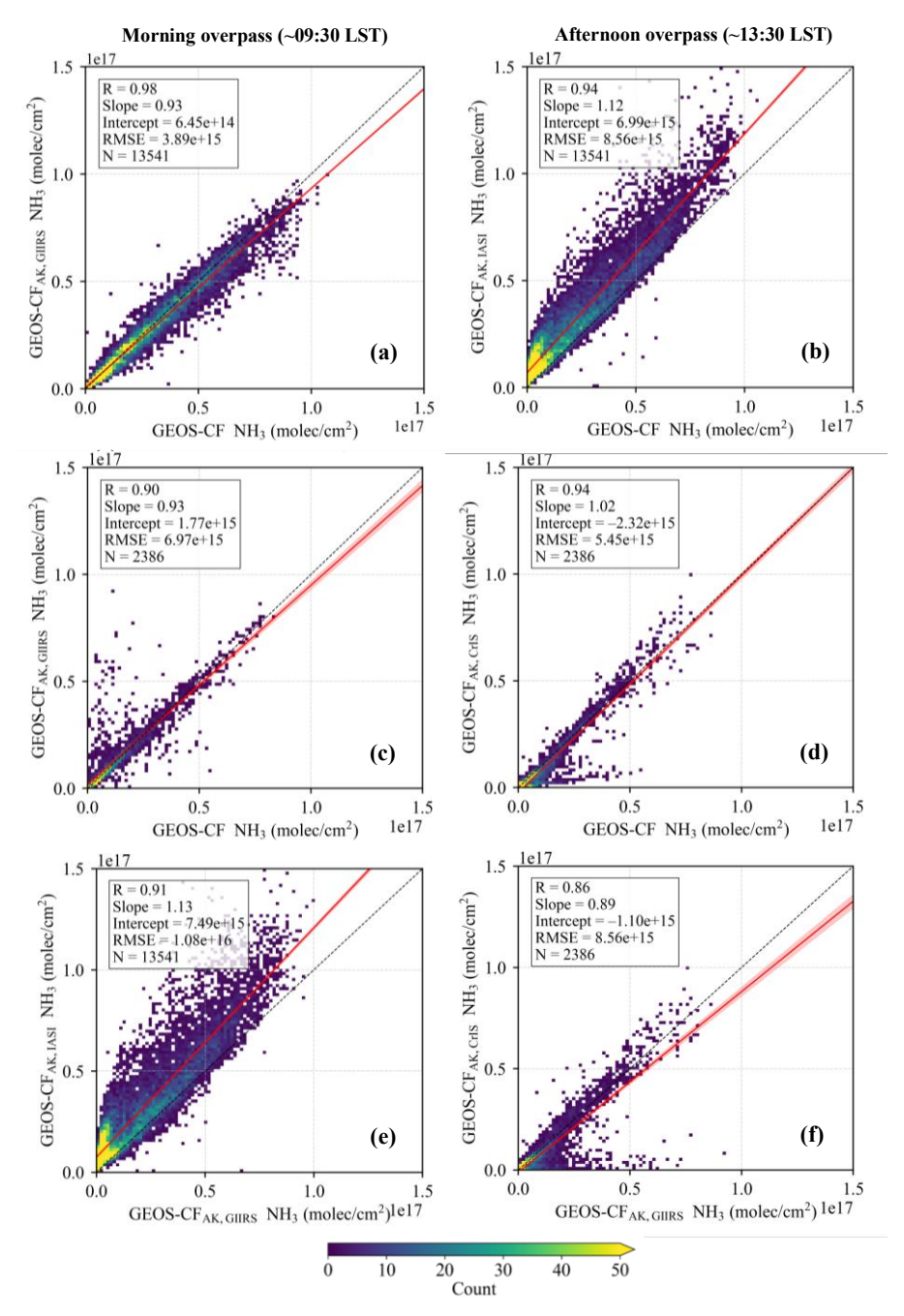


Figure S4. Comparison of the modelled NH₃ columns derived using satellite AVKs smoothing and those calculated without applying the AVKs over the North China Plain and the Northeast China Plain (30°-43°N, 110°-125°E) in June 2024. The data pairs are within the same grid cells and overpass times. (a) and (b) show the comparison of modelled NH₃ columns at morning overpass times after AVK smoothing for GHRS and IASI, respectively, with the original total column values. (c) and (d) are similar comparisons at afternoon overpass times for GHRS and CrIS, respectively. (e) and (f) show cross-comparisons between modelled NH₃ columns smoothed using different satellite AVKs.



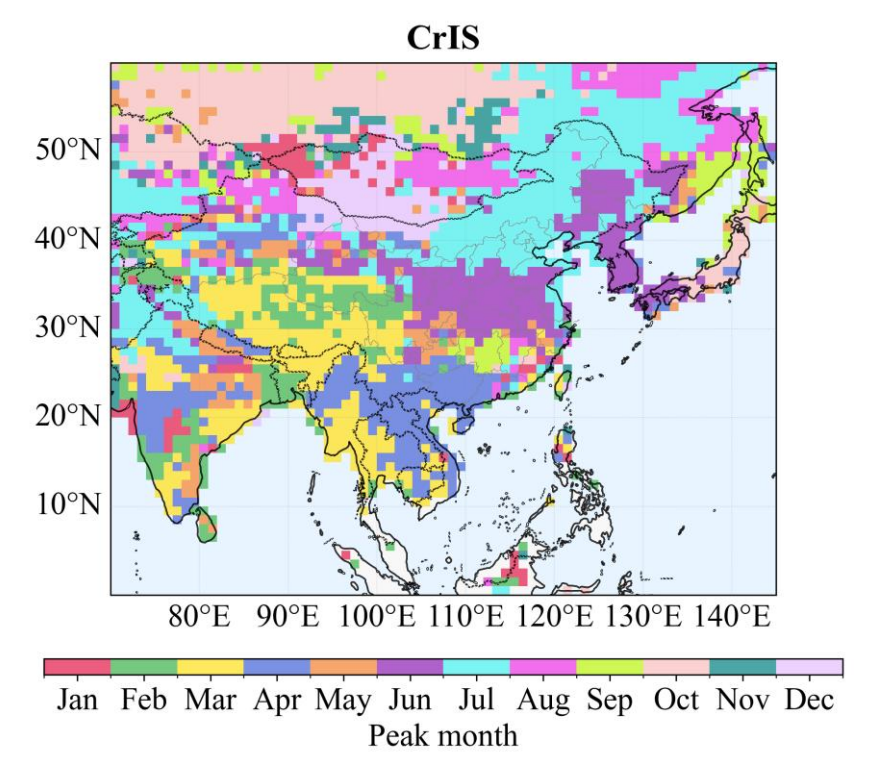


Figure S5. Same as Figure 5, but for CrIS retrievals from July 2022 to April 2025 at 1° grid.

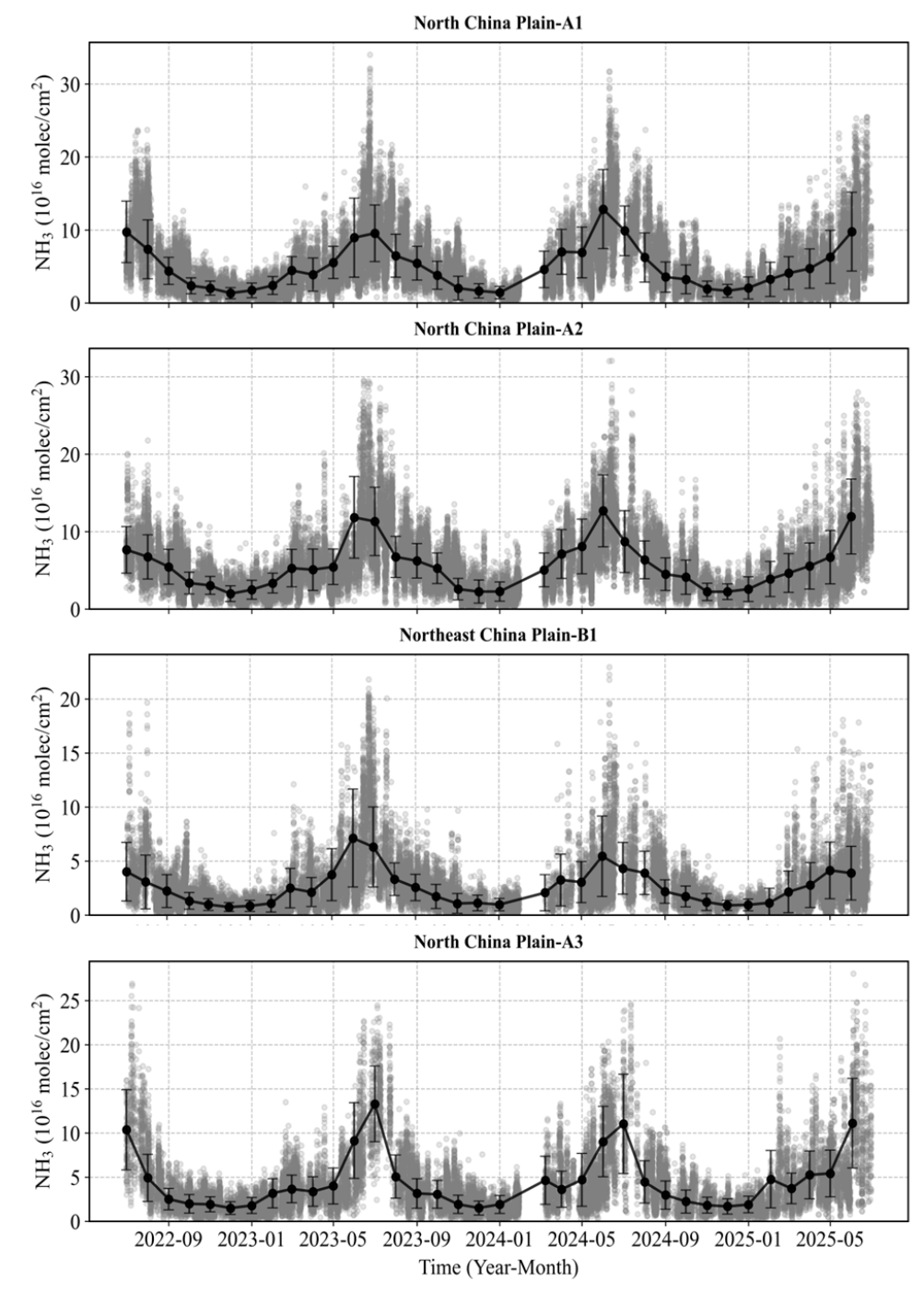


Figure S6. Monthly variations of NH₃ columns derived from GIIRS (July 2022–June 2025) for eight agricultural source areas.

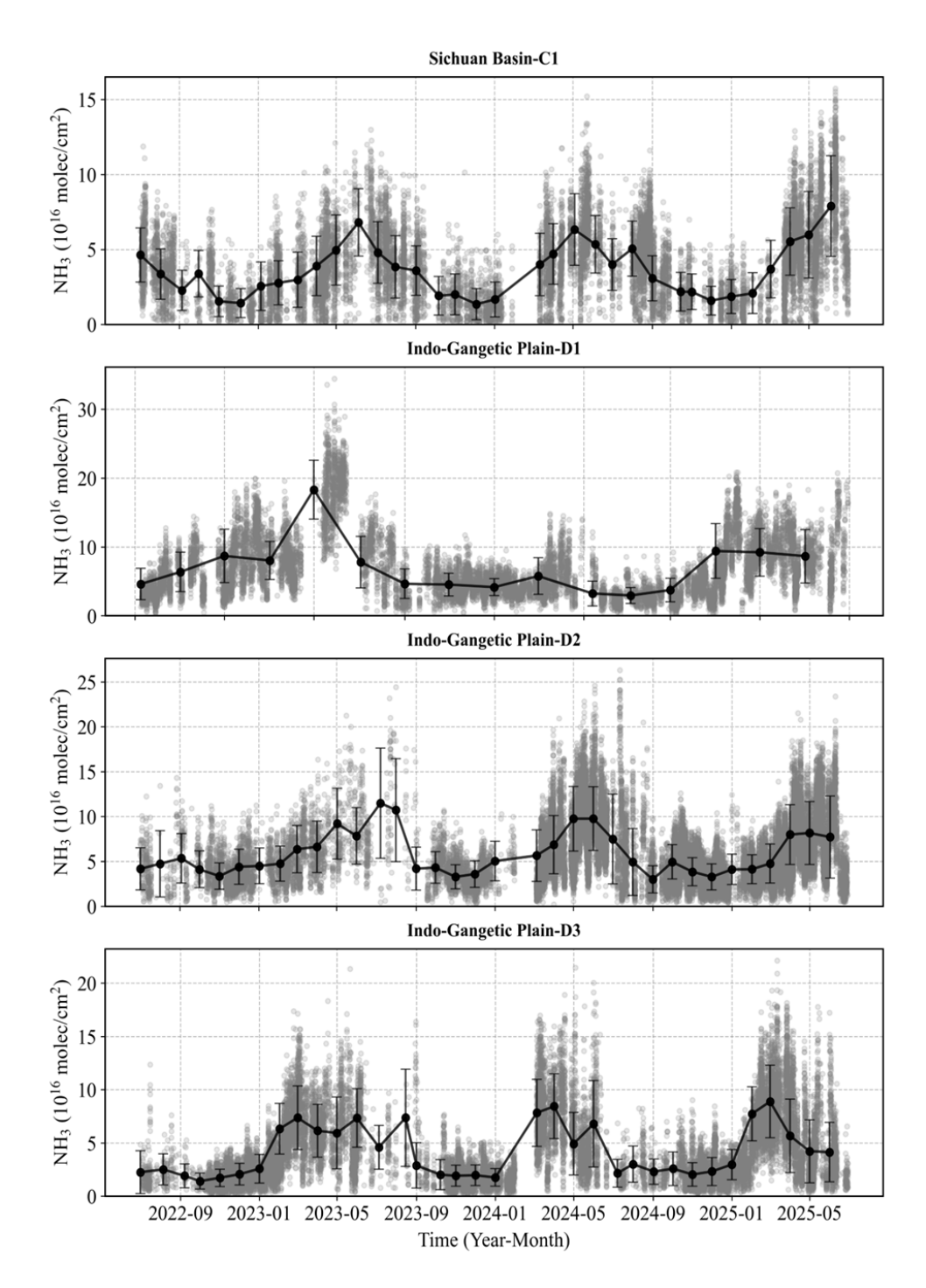


Figure S6 (continued). Monthly variations of NH₃ columns derived from GIRS (July 2022–June 2025) for eight agricultural source areas.

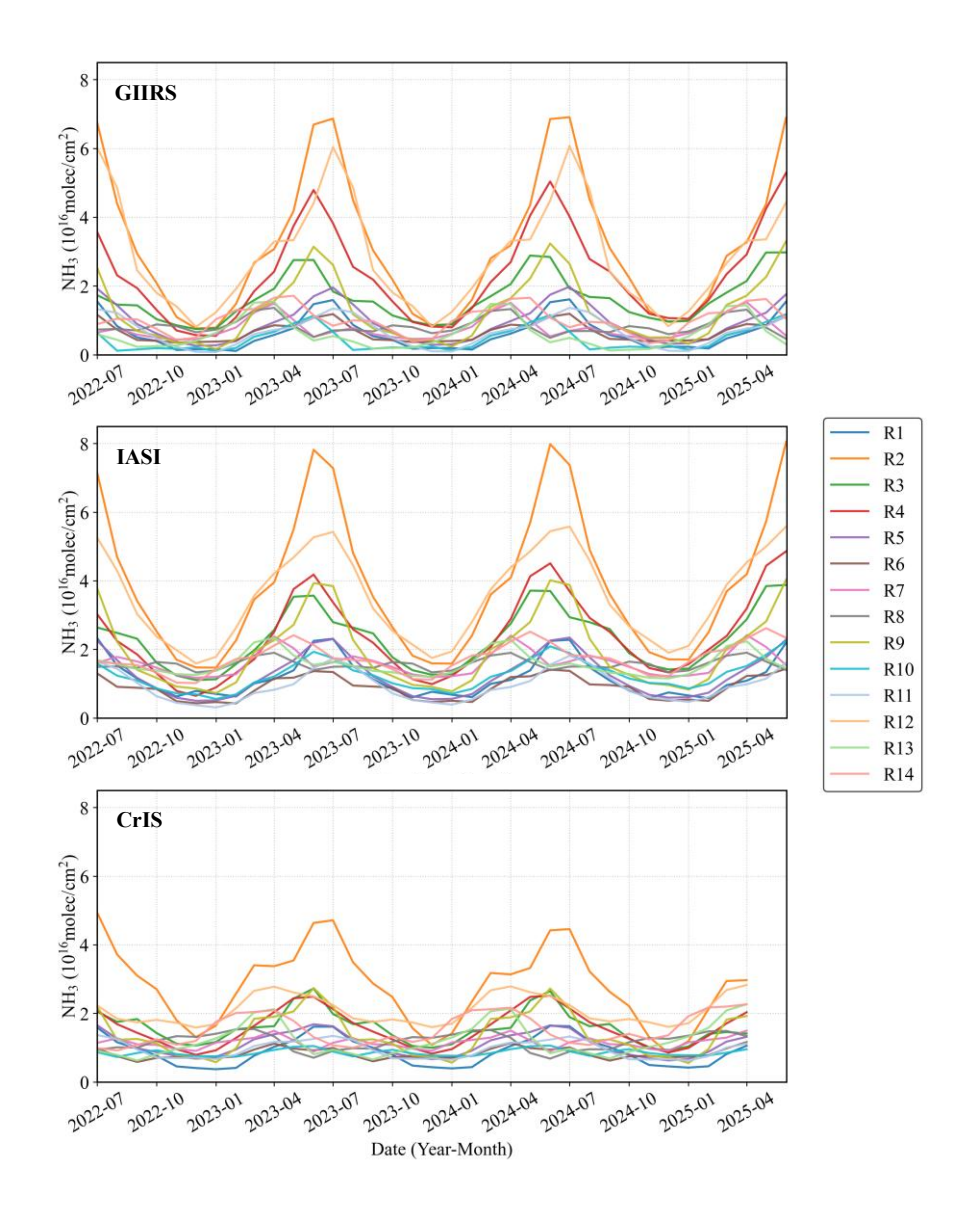


Figure S7. Monthly backgrounds of NH₃ columns derived from predefined regions using GIIRS (daytime overpass times, 7:00–19:00 LST), IASI (morning overpass times, ~9:30 LST), and CrIS observations (afternoon overpass times, ~13:30 LST).



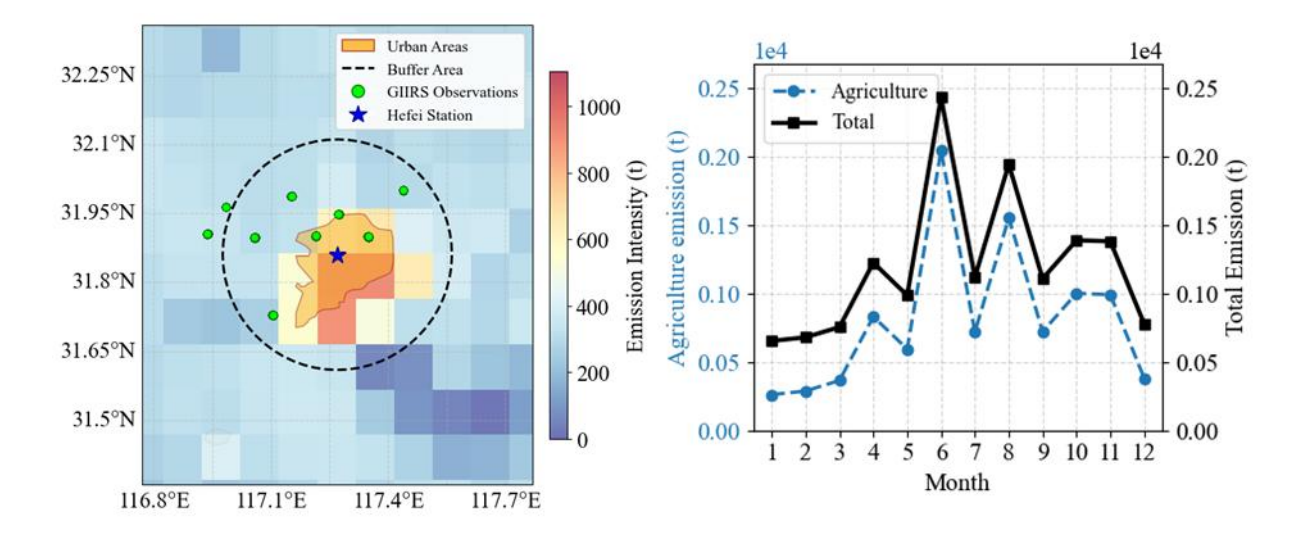


Figure S8. Spatial and temporal pattern of ammonia emissions in 2017 from the MIX emission inventory at the Hefei station. (a) Spatial distribution of anthropogenic NH₃ emissions and GIIRS observations; (b) Monthly timeseries of anthropogenic NH₃ emissions. The blue stars indicate the locations of Hefei station (31.91°N, 117.17°E) analyzed in Sect. 3.2.



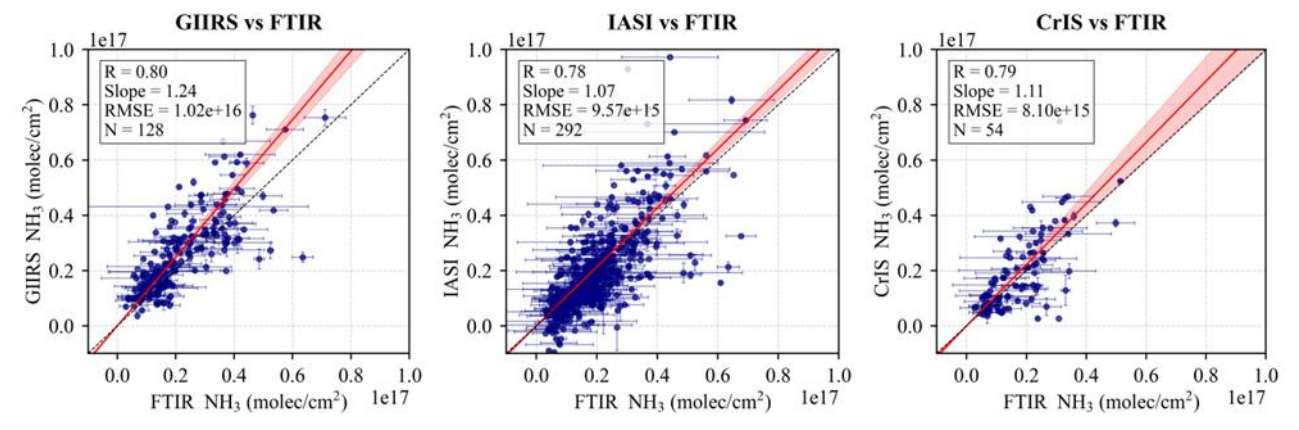


Figure S9. Same as Figure 8, but using the Orthogonal Distance Regression (ODR) method to fit hourly NH₃ columns from GIIRS, IASI, and CrIS to FTIR observations at the Hefei station.

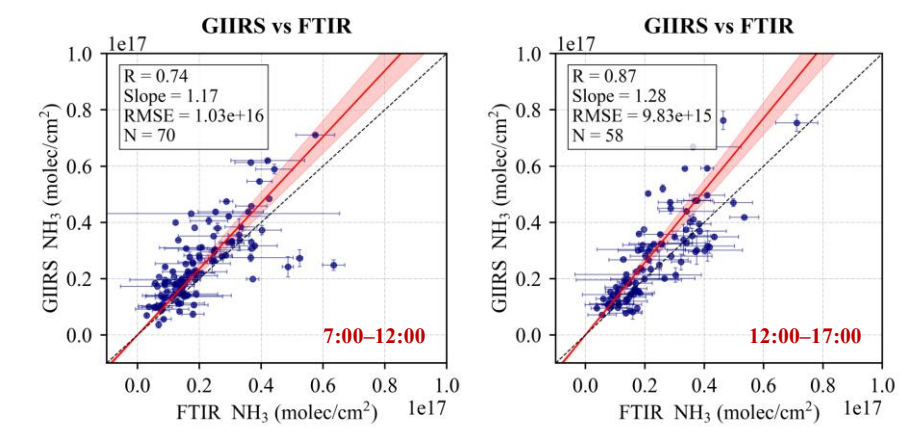


Figure S10. Cross-validation of GIIRS and FTIR from 8:00-12:00 and 12:00-16:00 using the Orthogonal Distance Regression (ODR) method.

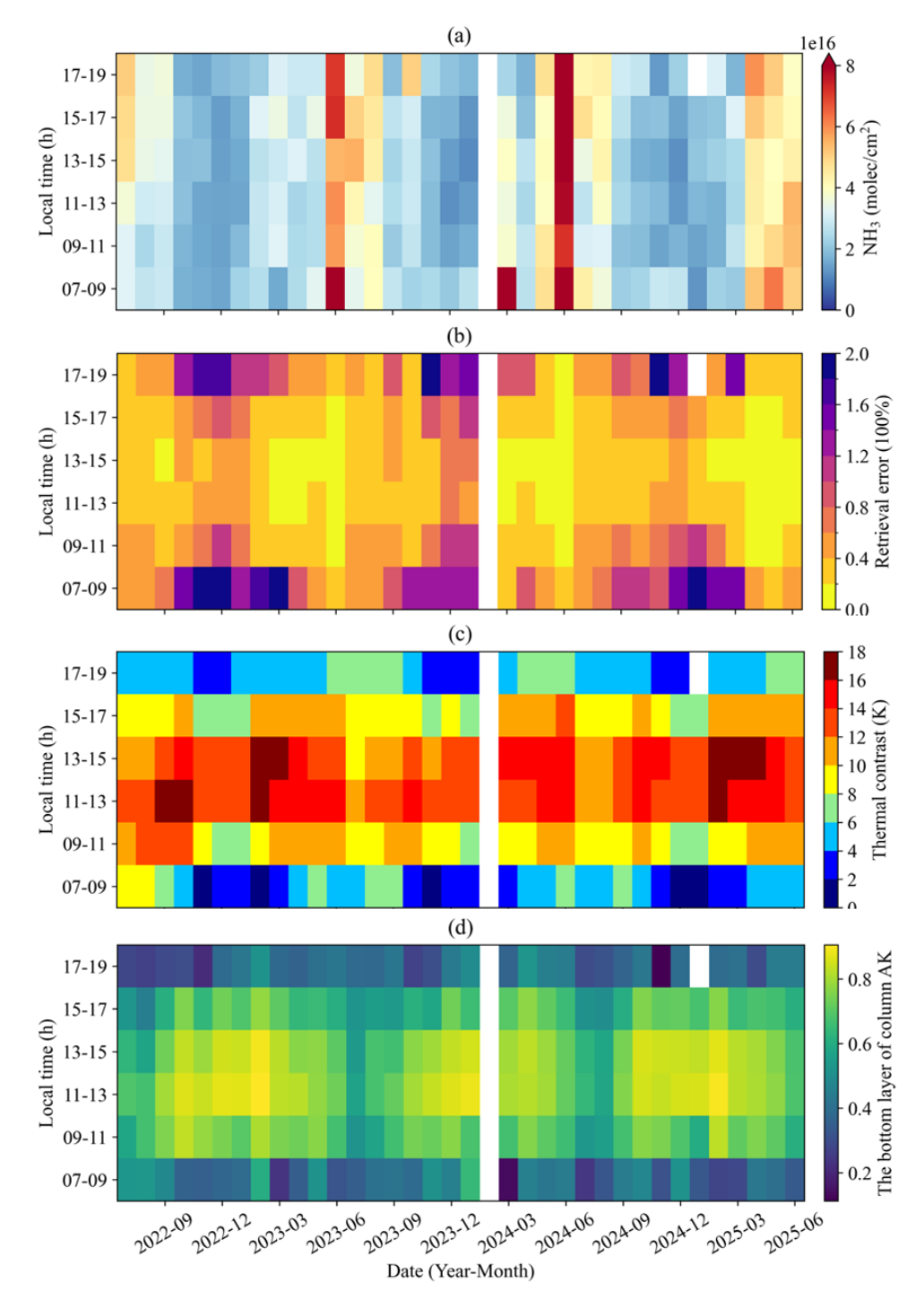
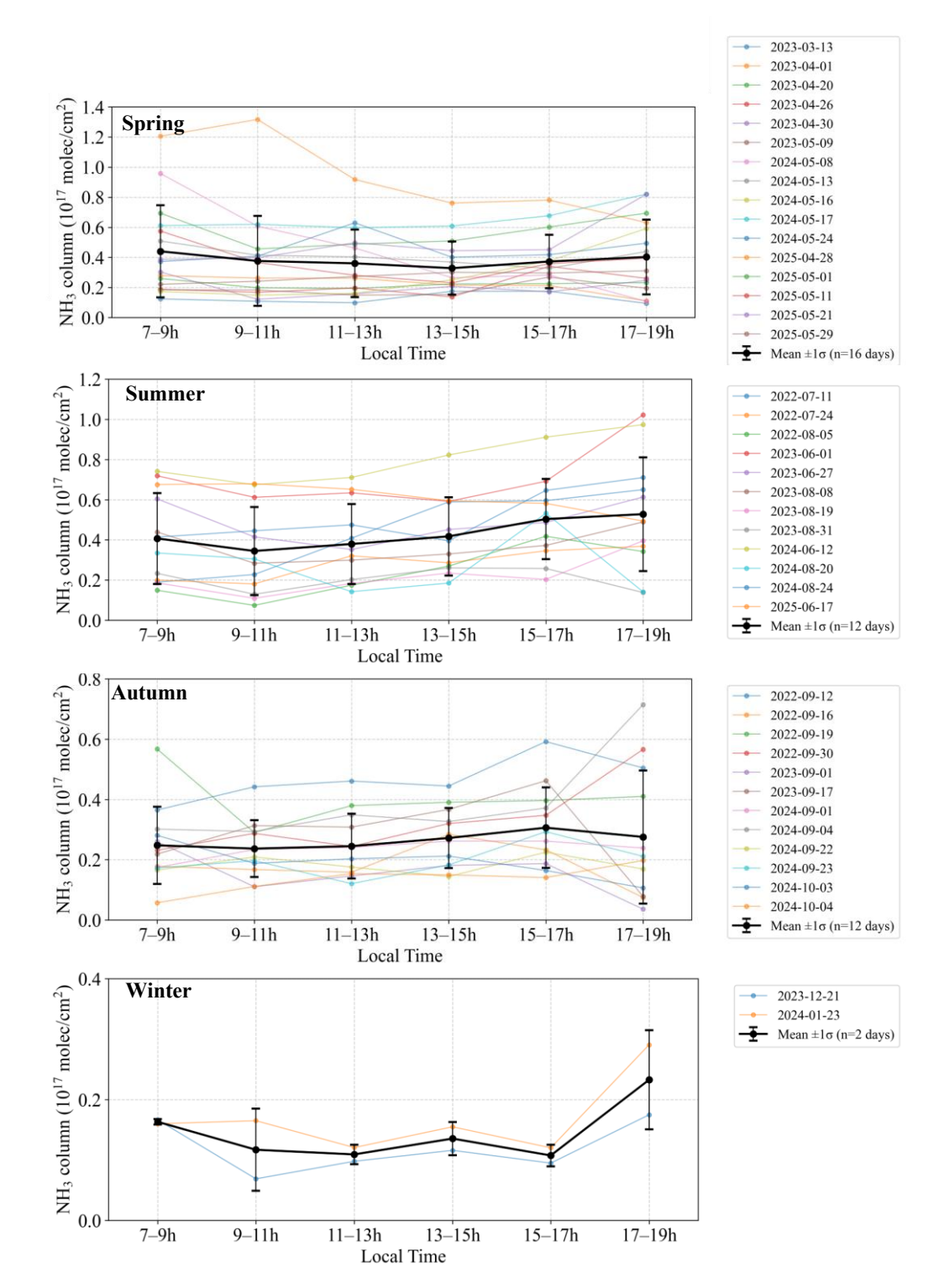


Figure S11. Temporal variations of (a) GIIRS-derived NH₃ columns, (b) the corresponding retrieval error, (c) TC, and (d) the bottom layer of column AVKs.



 $Figure~S12.~Day time~NH_3~variations~observed~by~FY-4B/GIIRS~from~37~high-quality~observation~days.\\$

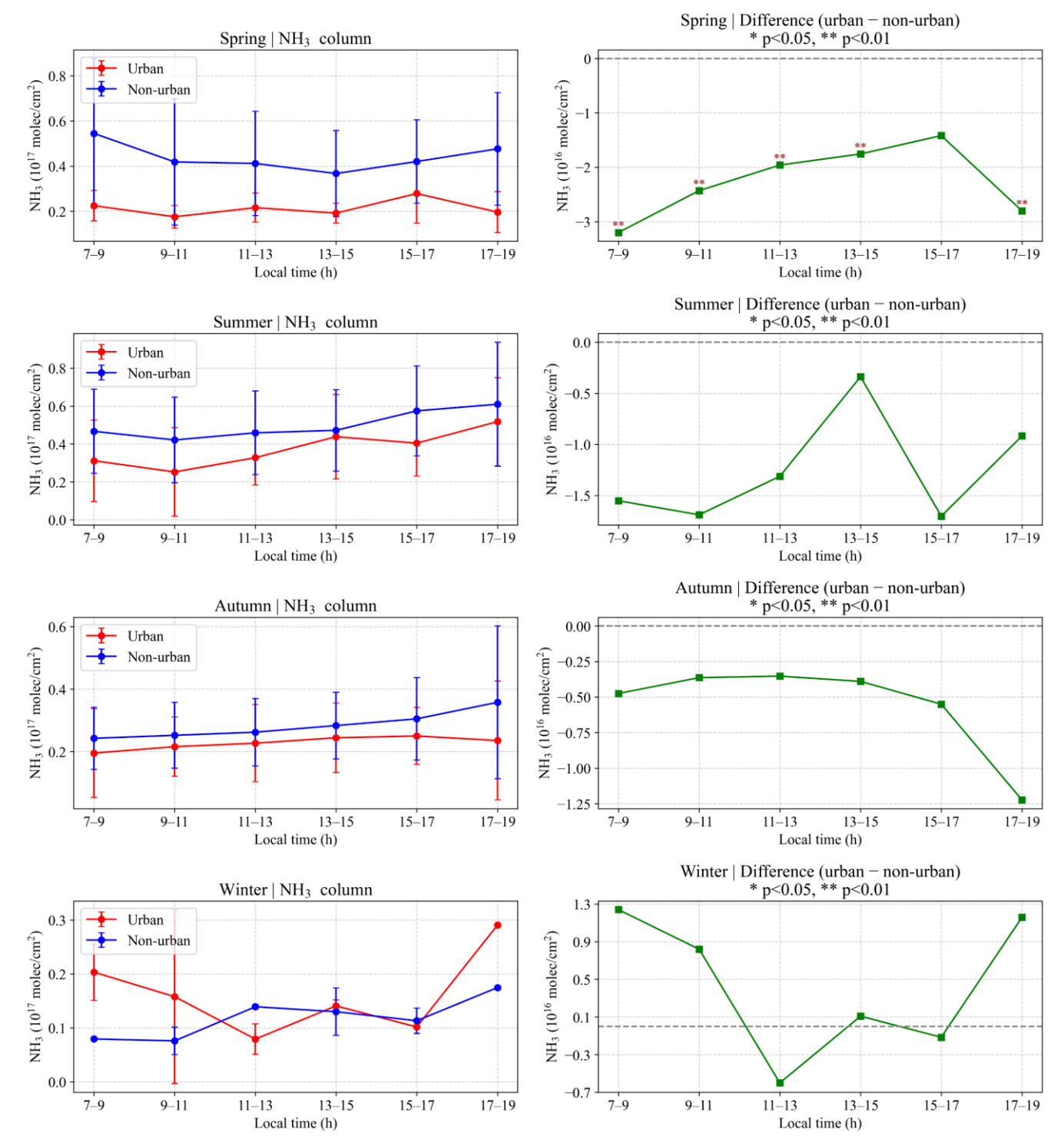


Figure S13. Daytime NH₃ variations observed by GHRS at the Hefei station in different seasons for urban areas and non-urban areas.



 $\begin{smallmatrix} 142\\ 143\end{smallmatrix}$

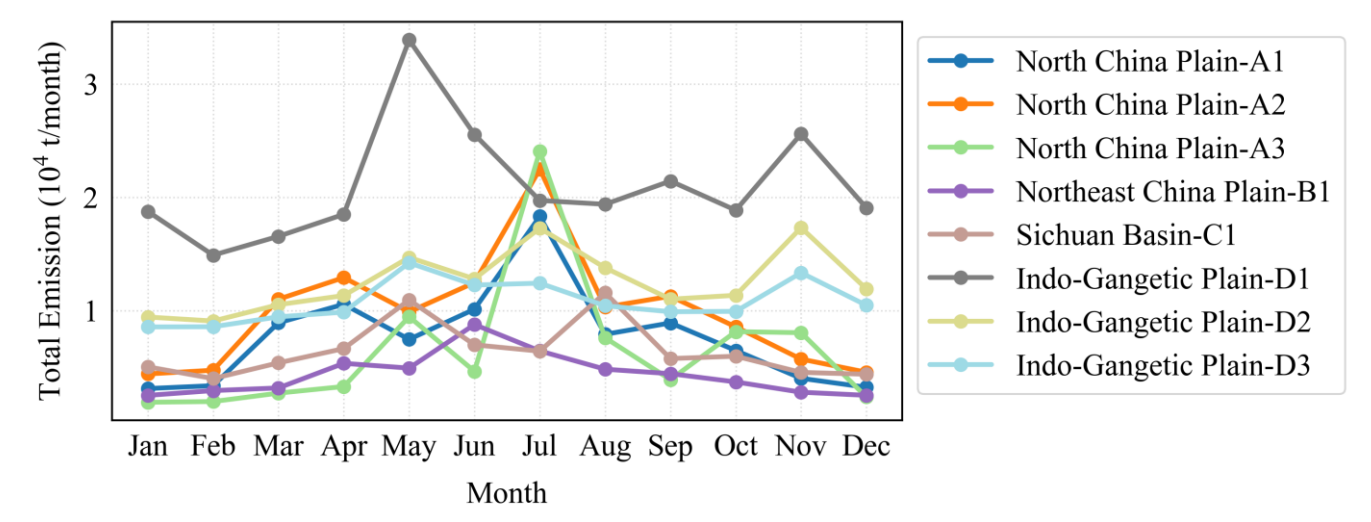


Figure S14. Monthly variations of NH₃ total emissions from the MIX inventory (2017) for eight agricultural source areas.

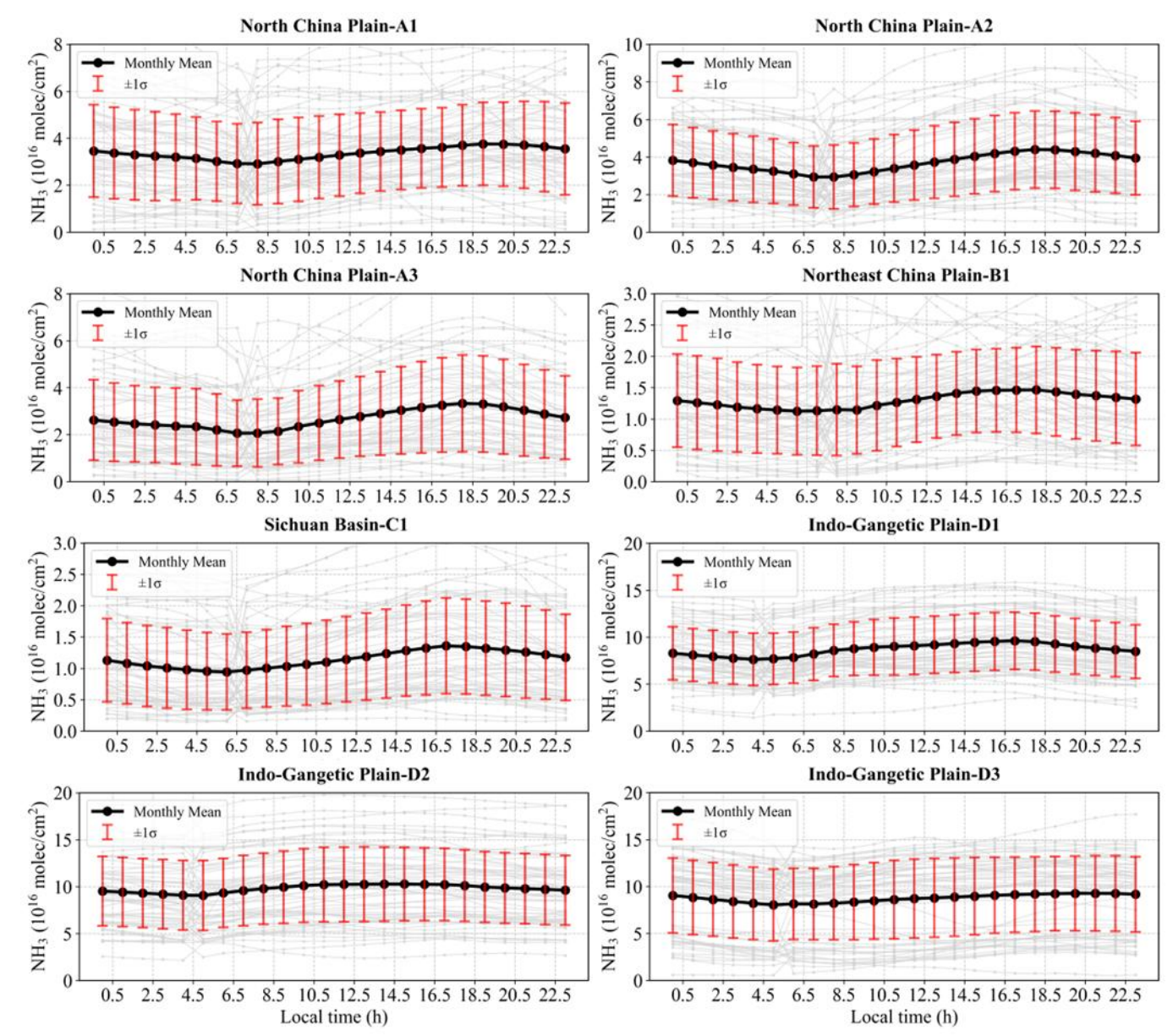


Figure S15. Diurnal NH3 variations in May and June 2025 from GEOS-CF model in the major agricultural areas.

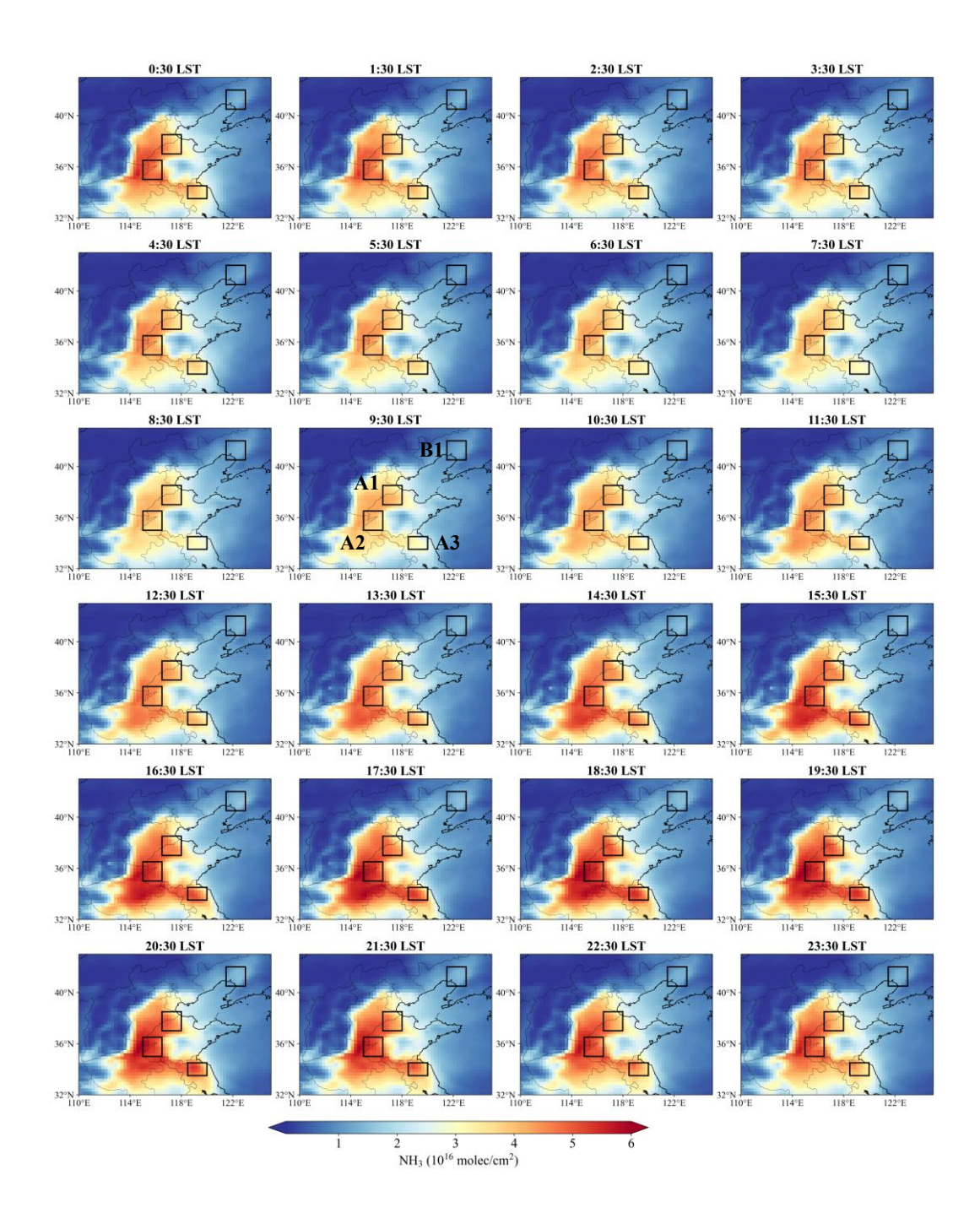


Figure S16. Spatial pattern of NH₃ columns from GEOS-CF model in May and June 2025 over the North China Plain and the Northeast China Plain.

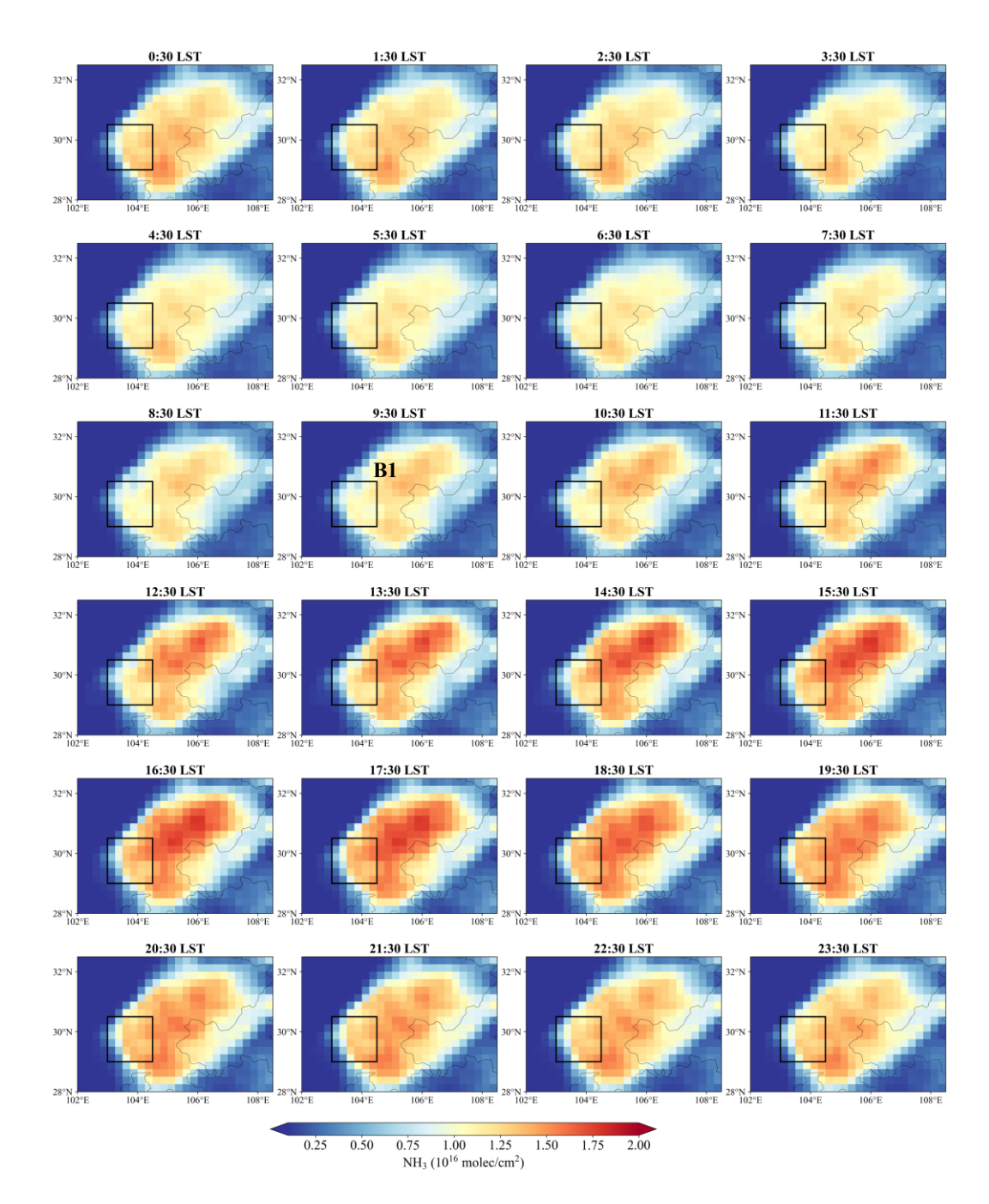


Figure S17. Spatial pattern of NH₃ columns from GEOS-CF model in May and June 2025 over the Sichuan Basin.

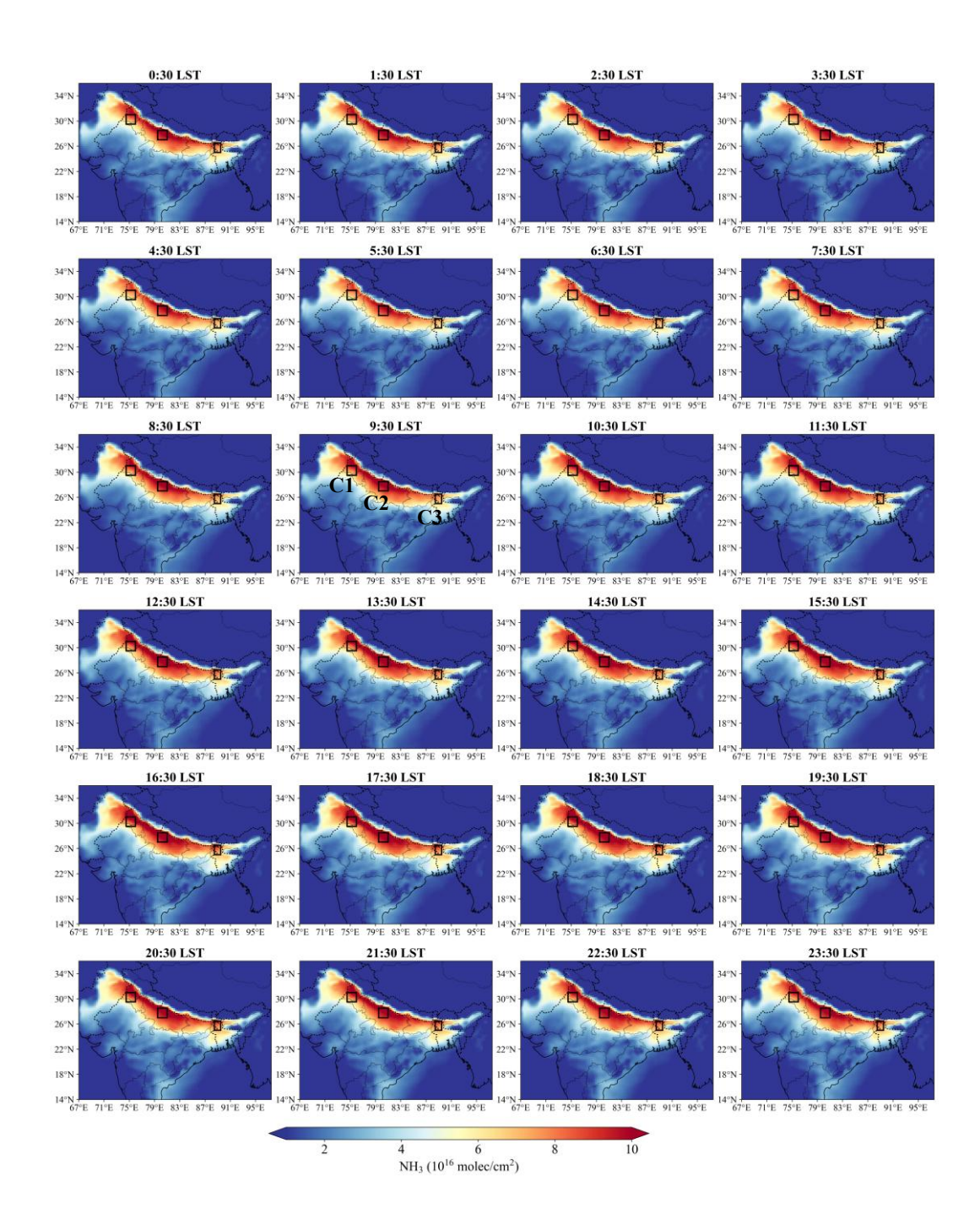


Figure S18. Spatial pattern of NH₃ columns from GEOS-CF model in May and June 2025 over the Indo-Gangetic Plain.

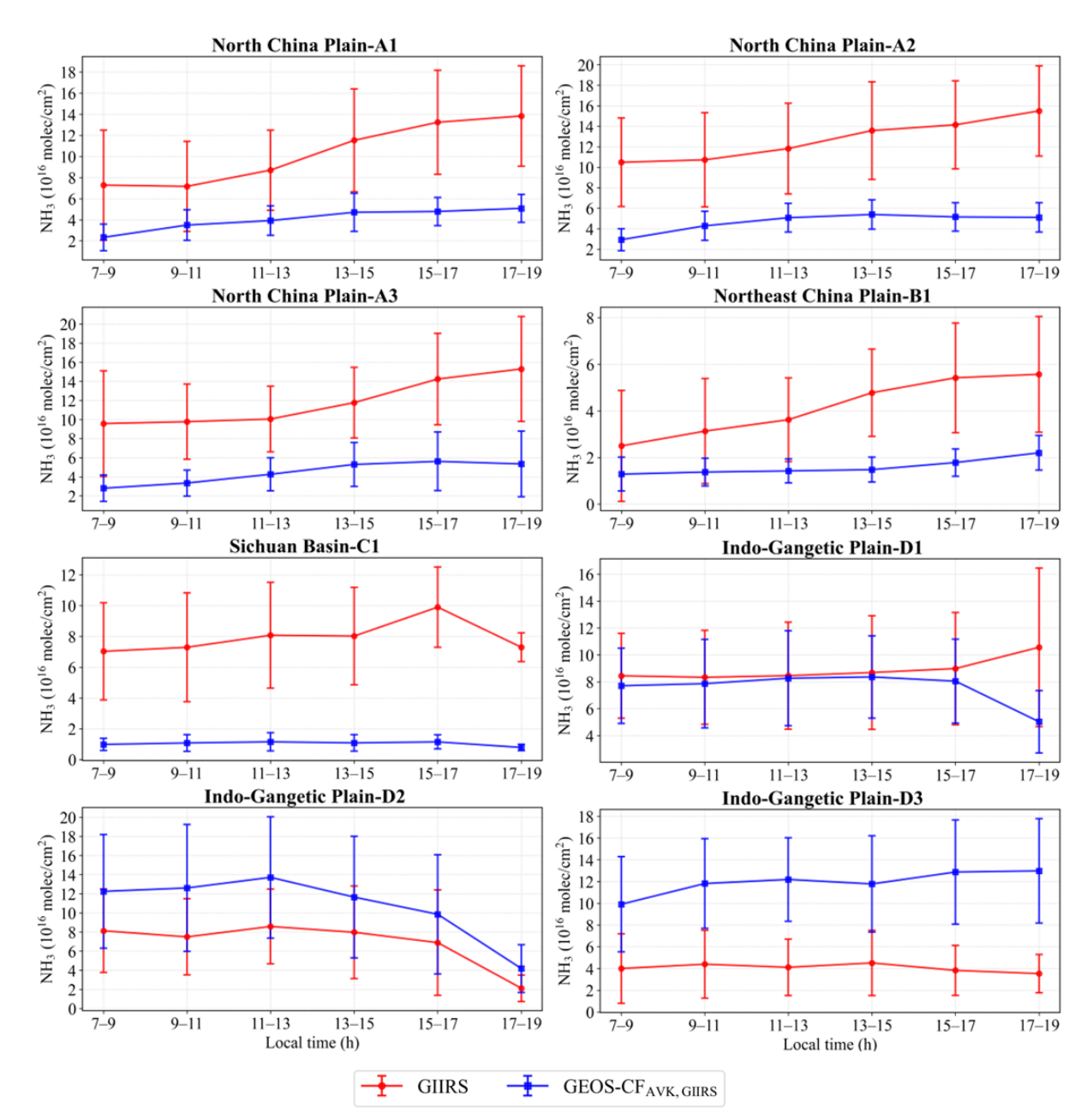


Figure S19. Diurnal NH₃ variations in May and June 2025 from GEOS-CF AVK-smoothed model data in the major agricultural areas.

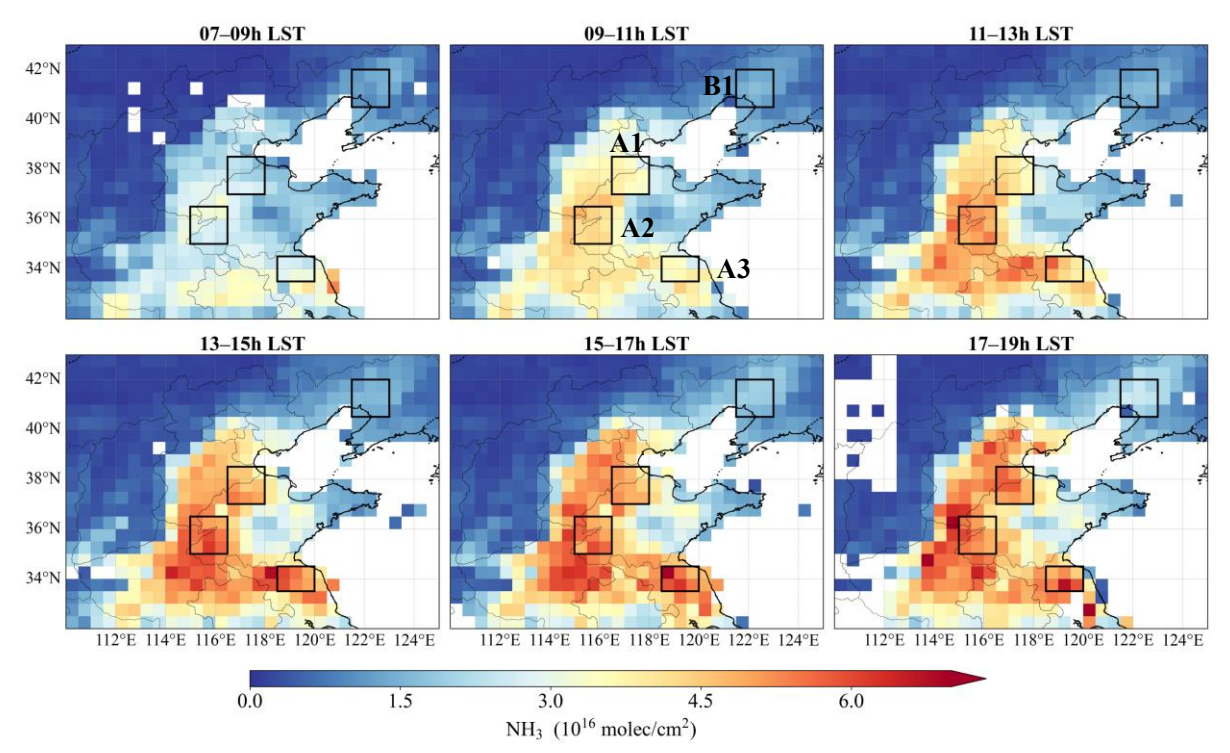


Figure S20. Spatial pattern of GEOS-CF AVK-smoothed model data in May and June 2025 over the North China Plain and the Northeast China Plain.

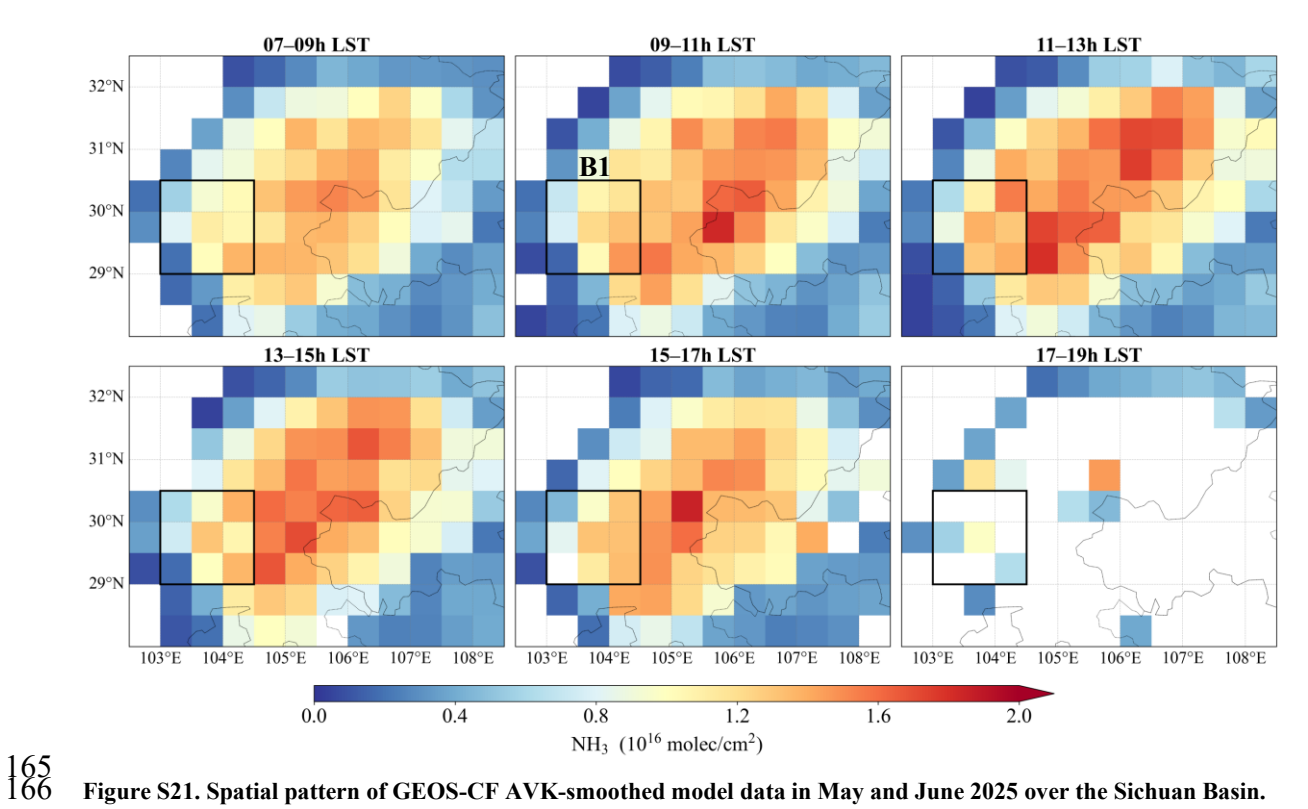


Figure S21. Spatial pattern of GEOS-CF AVK-smoothed model data in May and June 2025 over the Sichuan Basin.

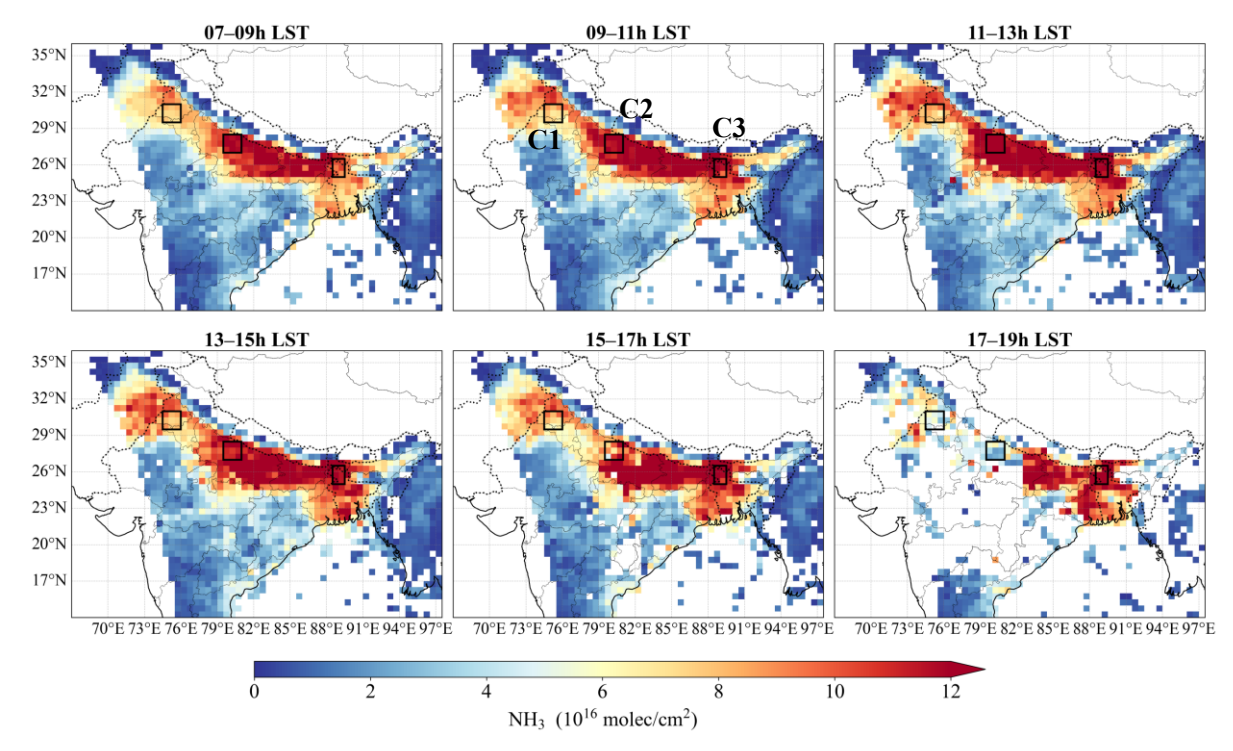


Figure S22. Spatial pattern of GEOS-CF AVK-smoothed model data in May and June 2025 over the Indo-Gangetic Plain.